

Free vibration of thermo-electro-mechanically postbuckled FG-CNTRC beams with geometric imperfections

Helong Wu^{1a}, Sritawat Kitipornchai^{1b} and Jie Yang^{*2}

¹ School of Civil Engineering, the University of Queensland, Brisbane, St. Lucia 4072, Australia

² School of Engineering, RMIT University, P.O. Box 71, Bundoora, VIC 3083, Australia

(Received February 5, 2018, Revised September 15, 2018, Accepted September 17, 2018)

Abstract. This paper investigates the free vibration of geometrically imperfect functionally graded carbon nanotube-reinforced composite (FG-CNTRC) beams that are integrated with two sur-face-bonded piezoelectric layers and subjected to a combined action of a uniform temperature rise, a constant actuator voltage and an in-plane force. The material properties of FG-CNTRCs are assumed to be temperature-dependent and vary continuously across the thick-ness. A generic imperfection function is employed to simulate various possible imperfections with different shapes and locations in the beam. The governing equations that account for the influence of initial geometric imperfection are derived based on the first-order shear deformation theory. The postbuckling configurations of FG-CNTRC hybrid beams are determined by the differential quadrature method combined with the modified Newton-Raphson technique, after which the fundamental frequencies of hybrid beams in the postbuckled state are obtained by a standard eigenvalue algorithm. The effects of CNT distribution pattern and volume fraction, geometric imperfection, thermo-electro-mechanical load, as well as boundary condition are examined in detail through parametric studies. The results show that the fundamental frequency of an imperfect beam is higher than that of its perfect counterpart. The influence of geometric imperfection tends to be much more pronounced around the critical buckling temperature.

Keywords: free vibration; postbuckling; functionally graded materials; carbon nanotube-reinforced composites; piezoelectric materials; thermo-electro-mechanical load

1. Introduction

Due to the superior mechanical properties, functionally graded carbon nanotube-reinforced composites (FG-CNTRCs) in which carbon nanotube (CNT) reinforcements are dispersed nonuniformly in the matrix have attracted considerable scientific and technological interests in the past few years (Liew *et al.* 2015, Shen 2009, Wu *et al.* 2015, 2016a). Owing to the graded variation of CNT concentration, the material properties of FG-CNTRCs exhibit a continuous change from one surface to the other, thus eliminating the interface problems that usually take place in conventional nanocomposites. By combining the outstanding properties of CNTs and the advantages of functionally graded materials (FGMs), FG-CNTRCs may find promising applications in aerospace and defence industries. Numerous research works have been done on the free vibration of FG-CNTRC structures. Among those, Ke *et al.* (2010) carried out nonlinear vibration analysis of FG-CNTRC beams based on Timoshenko beam theory. Yas and Samadi (2012) studied the free vibration of FG-CNTRC beams resting on an elastic foundation. Wattanasakulpong and Ungbhakorn (2013) analytically investigated the same

problem using various shear deformation theories. Shen and Xiang (2013) discussed the nonlinear vibration of FG-CNTRC beams resting on an elastic foundation in thermal environment. Lin and Xiang (2014a, b) examined the linear and nonlinear free vibrations of FG-CNTRC beams using p-Ritz method. Based on the two-dimensional elasticity theory, Nejati *et al.* (2016) presented the vibration analysis of FG-CNTRC beams under a compressive axial load. Wu *et al.* (2016b) extended the existing works to the geometrically imperfect FG-CNTRC beams and revealed that the initial geometric imperfection has an important effect on the nonlinear vibration behaviour.

The high-performance composite structures are often subjected to combined thermal and mechanical loads. The thermo-mechanically induced postbuckling deformation will change the structural configuration and influence the vibration characteristics that can ultimately affect the stability and control of those structures (Asadi *et al.* 2013, Esfahani *et al.* 2014, Komijani *et al.* 2013, 2014, Li *et al.* 2004, 2009, Rahimi *et al.* 2013). In spite of its practical importance, very limited work has been reported on the free vibration of postbuckled FG-CNTRC beams. Most recently, Shen *et al.* (2017) analysed the small- and large-amplitude vibration of thermally postbuckled FG-CNTRC beams resting on elastic foundations. With the exception of (Wu *et al.* 2016b), it appears that previous studies of the vibration behaviour have mainly focused on the perfect straight beams. In reality, geometric imperfection is inevitable in structural elements during their fabrication process and service life. As reported in Emam (2009), those geometric

*Corresponding author, Professor,

E-mail: j.yang@rmit.edu.au

^a Ph.D. Student, E-mail: helong.wu@uq.edu.au

^b Professor, E-mail: s.kitipornchai@uq.edu.au

imperfections have a considerable effect on the vibration characteristics of composite beams in the vicinity of postbuckling configuration. To the best of the authors' knowledge, so far there is no literature on the free vibration of geometrically imperfect FG-CNTRC beams under thermo-mechanical loads.

Owing to the electro-mechanical coupling effect, piezoelectric materials have been widely used as distributed actuators and sensors in smart structural system. The stability and vibration analyses of smart composite structures integrated with surface-mounted piezoelectric layers are of great practical importance for active structural control and health monitoring (Duan *et al.* 2010, Zhang *et al.* 2016). Rafiee *et al.* (2013a, b) investigated the nonlinear vibration and thermal buckling of piezoelectric FG-CNTRC beams under thermo-electric loads. Alibeigloo and Liew (2015) studied the bending and free vibration of FG-CNTRC beams integrated with piezoelectric actuator and sensor under an applied electric field. Yang *et al.* (2015) presented a dynamic buckling analysis of thermo-electro-mechanically loaded FG-CNTRC beams with surface-bonded piezoelectric layers. Wu *et al.* (2016c) dealt with the thermo-electro-mechanical post-buckling of piezoelectric FG-CNTRC beams with geometric imperfections.

This paper aims to investigate the free vibration of FG-CNTRC beams that are integrated with surface-bonded piezoelectric layers and subjected to thermo-electro-mechanical loads in both the pre- and post-buckling equilibrium states. Material properties of FG-CNTRCs are assumed to be graded in the thickness direction and estimated by the extended rule of mixture. A one-dimensional imperfection mode is used to model various possible geometric imperfections that may come in different shapes and locations in the beam. Parametric studies are conducted to highlight the effects of geometric imperfection mode, half-wave number, location and amplitude on the vibration response of piezoelectric FG-CNTRC beams. The influences of CNT distribution pattern and volume fraction, temperature rise, actuator voltage, in-plane force, and boundary condition are discussed as well. The thermal postbuckling of electro-mechanically prestressed piezoelectric FG-CNTRC beams is treated as a subset problem

2. Theoretical formulation

2.1 Effective material properties

Consider a piezoelectric CNTRC hybrid beam of length

L and total thickness H , as shown in Fig. 1(a). The hybrid beam consists of two piezoelectric layers of equal thickness h_p that are symmetrically bonded to the top and bottom surfaces of a CNTRC host of thickness h . The CNT reinforcements are assumed to be either functionally graded (FGX and FGO) or uniformly distributed (UD) along the thickness direction, with the volume fraction V_{cn}

$$\begin{aligned} \text{FGX: } V_{cn} &= 4 \frac{|z|}{h} V_{cn}^*, \\ \text{FGO: } V_{cn} &= \left(2 - 4 \frac{|z|}{h} \right) V_{cn}^*, \\ \text{UD: } V_{cn} &= V_{cn}^*. \end{aligned} \quad (1)$$

As illustrated in Fig. 1(b), the surfaces of FGX are CNT rich while this is inverted for FGO whose midplane is CNT rich. The CNT concentration is assumed to be constant across the thickness for UD. However, the total CNT volume fraction V_{cn}^* for the three distribution patterns of FGX, FGO and UD are the same to facilitate direct comparison.

The effective material properties of CNTRC that are graded across the thickness direction can be predicted by the extended rule of mixture (Shen 2009)

$$E_{11} = \eta_1 V_{cn} E_{11}^{cn} + V_m E_m, \quad (2)$$

$$\frac{\eta_2}{E_{22}} = \frac{V_{cn}}{E_{22}^{cn}} + \frac{V_m}{E_m}, \quad (3)$$

$$\frac{\eta_3}{G_{12}} = \frac{V_{cn}}{G_{12}^{cn}} + \frac{V_m}{G_m}, \quad (4)$$

$$\rho = V_{cn} \rho_{cn} + V_m \rho_m, \quad (5)$$

$$\nu_{12} = V_{cn} \nu_{12}^{cn} + V_m \nu_m, \quad (6)$$

where the superscript/subscript “cn” and “m” represent the CNT and matrix, respectively. E_{11}^{cn} , E_{22}^{cn} , E_m , G_{12}^{cn} , G_m are Young's and shear moduli; the volume fraction V_{cn} and V_m are related by $V_{cn} + V_m = 1$; ρ_{cn} and ρ_m are mass densities; ν_{12}^{cn} and ν_m are Poisson's ratios. η_i ($i = 1, 2, 3$) are the CNT efficiency parameters accounting for the size-dependence of the nanocomposites. The thermal expansion coefficient of CNTRC is given by

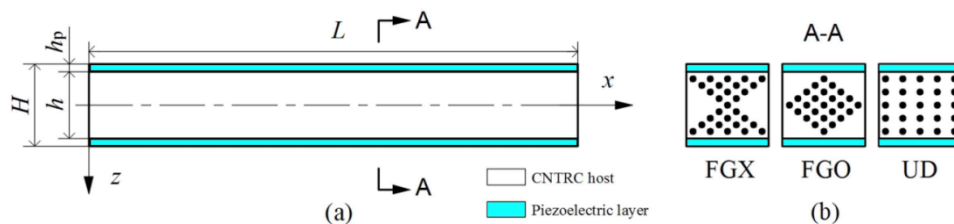


Fig. 1 Configuration and coordinate system of a piezoelectric CNTRC beam

$$\alpha_{11} = \frac{V_{cn} E_{11}^{cn} \alpha_{11}^{cn} + V_m E_m \alpha_m}{V_{cn} E_{11}^{cn} + V_m E_m}, \quad (7)$$

in which α_{12}^{cn} and α_m are thermal expansion coefficients of the CNT and matrix, respectively. By taking into consideration the temperature dependency, the effective material parameters of CNTRC given in Eqs. (2)-(7) are functions of both temperature and position.

2.2 Governing equations

Let the origin of coordinate system (X, Z) be located at the corner of mid-plane ($Z = 0$), with the coordinates X and Z along the length and thickness directions of the beam, respectively. Based on the first shear deformation theory (FSDT), the displacements of an arbitrary point in the hybrid beam parallel to X and Z directions are given by

$$\begin{aligned} \bar{U}(X, Z, t) &= U(X, t) + Z\psi(X, t), \\ \bar{W}(X, t) &= W(X) + W^*(X), \end{aligned} \quad (8)$$

where U and W are the longitudinal and transverse displacement components in the mid-plane, ψ is the angle of rotation of the normal to the mid-plane, t is the time. W^* is the initial geometric imperfection that may be either globally or locally distributed in the beam. The various possible imperfection shapes are simulated by a one-dimensional imperfection model (Wadee 2000, Wu *et al.* 2016b) that is the product of trigonometric and hyperbolic functions as

$$W^* = A_0 r \operatorname{sech}[a(x-c)] \cos[b\pi(x-c)], \quad (9)$$

in which $x = X/L$, $r = \sqrt{I/A}$ is the gyration radius of the beam cross section with A and I being the area and the second moment of the cross section; A_0 is the dimensionless

imperfection amplitude; a is the constant that determines the localization degree of the imperfection; b is the half-wave number of the imperfection that is symmetric about $x = c$. Table 1 lists the imperfection modes considered in this study, among which G_i and L_i ($i = 1, 2, 3, 4$) are global and localized imperfections, respectively.

It is assumed that the beam is initially stress free at a reference temperature T_0 then subjected to the combined action of a uniform temperature rise $\Delta T = T - T_0$, a constant actuator voltage V_Z and an in-plane force N_{X0} along the X -axis. In view of Eq. (8) and using Hamilton's principle, the nonlinear governing equations of the thermo-electro-mechanically loaded piezoelectric CNTRC beam which include the initial geometric imperfection can be expressed in terms of displacement components as



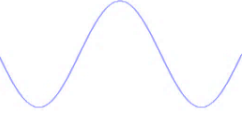


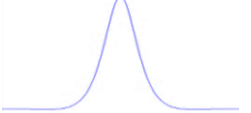
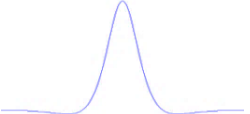
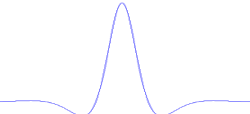
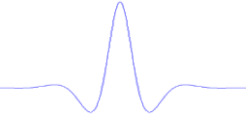
$$A_{11}(U_{,XX} + W_{,X}W_{,XX} + W_{,XX}W_{,X}^* + W_{,X}W_{,XX}^*) = I_1 \ddot{U}, \quad (10)$$

$$\begin{aligned} A_{55}(W_{,XX} + \psi_{,X}) + A_{11}(U_{,XX} + W_{,X}W_{,XX} \\ + W_{,XX}W_{,X}^* + W_{,X}W_{,XX}^*)(W_{,X} + W_{,X}^*) \\ + \left[A_{11}U_{,X} + \frac{1}{2}A_{11}(W_{,X})^2 + A_{11}W_{,X}W_{,X}^* \right. \\ \left. - N_X^T - N_X^E - N_{X0} \right](W_{,XX} + W_{,XX}^*) = I_1 \ddot{W}, \end{aligned} \quad (11)$$

$$D_{11}\psi_{,XX} - A_{55}(W_{,X} + \psi) = I_3 \ddot{\psi}, \quad (12)$$

where a comma and an overdot denote the partial derivative with respect to the coordinate X and time t , respectively. It should be noted that for a uniform temperature change and a constant actuator voltage, the derivatives of thermo-electrically induced forces with respect to X as well as the thermo-electrically induced moments vanish, hence are omitted in the governing equations. The thermally and electrically induced forces N_X^T and N_X^E are determined by

Table 1 Imperfection modes (Wu *et al.* 2016b)

		
Sine-type $a = 0, b = 1, c = 0.5$	G1-mode $a = 0, b = 2, c = 0.5$	G2-mode $a = 0, b = 3, c = 0.5$
		
G3-mode $a = 0, b = 5, c = 0.5$	G4-mode $a = 0, b = 7, c = 0.5$	L1-mode $a = 15, b = 2, c = 0.5$
		
L2-mode $a = 15, b = 3, c = 0.5$	L3-mode $a = 15, b = 5, c = 0.5$	L4-mode $a = 15, b = 7, c = 0.5$

$$N_X^T = \int_{-H/2}^{-h/2} Q_{11}^p \alpha_p \Delta T dZ + \int_{-h/2}^{h/2} Q_{11}^h \alpha_{11} \Delta T dZ + \int_{h/2}^H Q_{11}^p \alpha_p \Delta T dZ, \quad (13)$$

$$N_X^E = \int_{-H/2}^{-h/2} Q_{11}^p d_{31} E_Z dZ + \int_{h/2}^H Q_{11}^p d_{31} E_Z dZ. \quad (14)$$

The stiffness components and inertia related terms are defined as

$$(A_{11}, D_{11}) = \int_{-H/2}^{-h/2} Q_{11}^p (1, Z^2) dZ + \int_{-h/2}^{h/2} Q_{11}^h (1, Z^2) dZ + \int_{h/2}^H Q_{11}^p (1, Z^2) dZ, \quad (15)$$

$$A_{55} = \kappa \left(\int_{-H/2}^{-h/2} Q_{55}^p dZ + \int_{-h/2}^{h/2} Q_{55}^h dZ + \int_{h/2}^H Q_{55}^p dZ \right), \quad (16)$$

$$(I_1, I_3) = \int_{-H/2}^{-h/2} \rho_p (1, Z^2) dZ + \int_{-h/2}^{h/2} \rho (1, Z^2) dZ + \int_{h/2}^H \rho_p (1, Z^2) dZ. \quad (17)$$

In the above equations, the elastic constants Q_{11}^h , Q_{11}^p , Q_{55}^h , Q_{55}^p , with superscripts “h” and “p” referring to the CNTRC host and piezoelectric layer respectively, are given by

$$(Q_{11}^h, Q_{11}^p) = (E_{11}/(1-\nu_{12}\nu_{21}), E_p/(1-\nu_p^2)), \quad (18)$$

$$(Q_{55}^h, Q_{55}^p) = (G_{13}, E_p/2(1+\nu_p))$$

where E_p , ρ_p , ν_p , α_p and d_{31} are the Young's modulus, mass density, Poisson's ratio, thermal expansion coefficient and piezoelectric strain constant of the piezoelectric layer, respectively. $E_Z = V_Z/h_p$ is the electric field due to the applied actuator voltage.

Neglecting inertia related terms in Eqs. (10)-(12) leads to the following equations governing the static postbuckling of piezoelectric CNTRC beams under thermo-electro-mechanical loading

$$A_{11}(U_{,xx} + W_{,x}W_{,xx} + W_{,xx}W_{,x}^* + W_{,x}W_{,xx}^*) = 0, \quad (19)$$

$$A_{55}(W_{,xx} + \psi_{,x}) + \left[A_{11}U_{,x} + \frac{1}{2}A_{11}(W_{,x})^2 + A_{11}W_{,x}W_{,x}^* - N_X^T - N_X^E - N_{X0} \right] (W_{,xx} + W_{,xx}^*) = 0, \quad (20)$$

$$D_{11}\psi_{,xx} - A_{55}(W_{,x} + \psi) = 0, \quad (21)$$

Let (U_0, W_0, ψ_0) denote the static postbuckling solutions of Eqs. (19)-(21). By substituting for (U, W, ψ) in Eqs. (10)-(12) with $(U+U_0, W+W_0, \psi+\psi_0)$, we obtain the governing equations of motion for the thermo-electro-mechanically postbuckled piezoelectric CNTRC beam as

$$A_{11}(U_{,xx} + W_{,x}W_{,xx} + W_{,xx}W_{,x}^* + W_{,x}W_{,xx}^* + W_{,xx}W_{0,x} + W_{,x}W_{0,xx}) = I_1\ddot{U}, \quad (22)$$

$$A_{55}(W_{,xx} + \psi_{,x}) + \left[A_{11}U_{0,x} + \frac{1}{2}A_{11}(W_{0,x})^2 + A_{11}W_{0,x}W_{,x}^* - N_X^T - N_X^E - N_{X0} \right] W_{,xx} + A_{11} \left[U_{,x} + \frac{1}{2}(W_{,x})^2 + W_{,x}W_{0,x} + W_{,x}W_{,x}^* \right] (W_{,xx} + W_{0,xx} + W_{,xx}^*) = I_1\ddot{W}, \quad (23)$$

$$D_{11}\psi_{,xx} - A_{55}(W_{,x} + \psi) = I_3\ddot{\psi}. \quad (24)$$

In this study, the beam is either hinged or clamped at each end, with the associated boundary conditions as follows

$$\text{Hinged (H): } U = 0, \quad W = 0, \quad D_{11}\psi_{,x} = 0; \quad (25)$$

$$\text{Clamped (C): } U = 0, \quad W = 0, \quad \psi = 0. \quad (26)$$

By introducing the following dimensionless parameters

$$x = X/L, \quad (u, w, u_0, w_0, w^*) = (U, W, U_0, W_0, W^*)/r, \quad (\varphi, \varphi_0) = (\psi, \psi_0),$$

$$\eta = r/L, \quad (a_{11}, a_{55}, d_{11}) = (A_{11}, A_{55}, D_{11}/r^2)/A_{110},$$

$$\eta = r/L, \quad (a_{11}, a_{55}, d_{11}) = (A_{11}, A_{55}, D_{11}/r^2)/A_{110}, \quad (27)$$

$$(I_a, I_c) = \{I_1, I_3/r^2\}/I_{10},$$

$$(P^T, P^E, P) = (N_X^T, N_X^E, N_{X0})/A_{110},$$

$$\tau = t\sqrt{A_{110}/I_{00}}/L,$$

$$\omega = \Omega L\sqrt{I_{00}/A_{110}},$$

in which A_{110} and I_{10} are the values of A_{11} and I_1 of the equivalent homogeneous beam made from the pure matrix material, the static governing Eqs. (19)-(21) can be rewritten in the dimensionless form as

$$a_{11}u_{,xx} + a_{11}\eta(w_{,x}w_{,xx} + w_{,xx}w_{,x}^* + w_{,x}w_{,xx}^*) = 0, \quad (28)$$

$$a_{55}(w_{,xx} + \frac{1}{\eta}\varphi_{,x}) + \left[a_{11}u_{,x} + \frac{1}{2}a_{11}\eta^2(w_{,x})^2 + a_{11}\eta^2w_{,x}w_{,x}^* - P^T - P^E - P \right] (w_{,xx} + w_{,xx}^*) = 0, \quad (29)$$

$$d_{11}\varphi_{,xx} - \frac{a_{55}}{\eta}(w_{,x} + \frac{1}{\eta}\varphi) = 0 \quad (30)$$

The governing equations of motion (22)-(24) can be nondimensionalized as

$$a_{11}u_{,xx} + a_{11}\eta(w_{,x}w_{,xx} + w_{,xx}w_{,x}^* + w_{,x}w_{,xx}^* + w_{,xx}w_{0,x} + w_{,xx}w_{0,xx}^*) = I_a \ddot{u}, \quad (31)$$

$$\begin{aligned} a_{55}\left(w_{,xx} + \frac{1}{\eta}\varphi_{,x}\right) + \left[a_{11}\eta u_{0,x} + \frac{1}{2}a_{11}\eta^2(w_{0,x})^2 + a_{11}\eta^2 w_{0,x}w_{,x}^* - P^T - P^E - P\right]w_{,xx} \\ + a_{11}\eta(u_{,xx} + \eta w_{,x}w_{,xx} + \eta w_{,xx}w_{,x}^* + \eta w_{,x}w_{,xx}^* + \eta w_{,xx}w_{0,x} + \eta w_{,xx}w_{0,xx}^*)(w_{,x} + w_{0,x} + w_{,x}^*) \\ + a_{11}\eta\left[u_{,x} + \frac{1}{2}\eta(w_{,x})^2 + \eta w_{,x}w_{0,x} + \eta w_{,x}w_{,x}^*\right] \\ (w_{,xx} + w_{0,xx} + w_{,xx}^*) = I_a \ddot{w}, \end{aligned} \quad (32)$$

$$d_{11}\varphi_{,xx} - \frac{1}{\eta}a_{55}(w_{,x} + \varphi) = I_c \ddot{\varphi}. \quad (33)$$

The boundary conditions in Eqs. (25) and (26) can be handled in the same way as

$$\text{Hinged (H): } u = 0, \quad w = 0, \quad d_{11}\varphi_x = 0; \quad (34)$$

$$\text{Clamped (C): } u = 0, \quad w = 0, \quad \varphi = 0. \quad (35)$$

2.3 Solution procedure

The differential quadrature (DQ) method is employed to convert the partial differential governing equations into a set of algebraic equations that is then solved through an iterative procedure. According to DQ rule, the unknown displacement components u , w , φ and their k^{th} partial differentiation with respect to x are approximated by

$$\begin{aligned} \{u, w, \varphi\} &= \sum_{m=1}^N l_m(x) \{u_m, w_m, \varphi_m\}, \\ \text{and } \frac{\partial^k}{\partial x^k} \{u, w, \varphi\} \Big|_{x=x_i} &= \sum_{m=1}^N C_{im}^{(k)} \{u_m, w_m, \varphi_m\}, \end{aligned} \quad (36)$$

where $l_m(x)$ is the Lagrange interpolation polynomials; $\{u_m, w_m, \varphi_m\}$ are the values of $\{u, w, \varphi\}$ at $x = x_m$; $C(k)_{im}$ is the weight coefficient of the k^{th} partial differentiation of unknown displacements with respect to x and can be determined by a recurrence scheme (Yang *et al.* 2006); N is the total number of grid points that are distributed along the x direction in a cosine pattern as

$$x_i = \left\{1 - \cos\left[\pi(i-1)/(N-1)\right]\right\}/2, \quad i = 1, 2, \dots, N. \quad (37)$$

Applying the relationships (36) to the static governing Eqs. (28)-(30) yields

$$a_{11} \sum_{m=1}^N C_{im}^{(2)} u_m + a_{11}\eta \left(\sum_{m=1}^N C_{im}^{(1)} w_m \sum_{m=1}^N C_{im}^{(2)} w_m \right. \quad (38)$$

$$\left. + \sum_{m=1}^N C_{im}^{(2)} w_m \sum_{m=1}^N C_{im}^{(1)} w_m^* + \sum_{m=1}^N C_{im}^{(1)} w_m \sum_{m=1}^N C_{im}^{(2)} w_m^* \right) = 0 \quad (38)$$

$$\begin{aligned} \left[a_{11}\eta \sum_{m=1}^N C_{im}^{(1)} u_m + \frac{a_{11}\eta^2}{2} \left(\sum_{m=1}^N C_{im}^{(1)} w_m \right)^2 + a_{11}\eta^2 \sum_{m=1}^N C_{im}^{(1)} w_m \sum_{m=1}^N C_{im}^{(1)} w_m^* - P^T - P^E - P \right] \end{aligned} \quad (39)$$

$$\left(\sum_{m=1}^N C_{im}^{(2)} w_m + \sum_{m=1}^N C_{im}^{(2)} w_m^* \right) + a_{55} \left(\sum_{m=1}^N C_{im}^{(2)} w_m + \frac{1}{\eta} \sum_{m=1}^N C_{im}^{(1)} \varphi_m \right) = 0,$$

$$d_{11} \sum_{m=1}^N C_{im}^{(2)} \varphi_m - \frac{a_{55}}{\eta} \left(\sum_{m=1}^N C_{im}^{(1)} w_m + \frac{1}{\eta} \varphi_i \right) = 0. \quad (40)$$

Similarly, the governing equations of motion (31)-(33) of postbuckled hybrid beams can be discretized as

$$\begin{aligned} a_{11} \sum_{m=1}^N C_{im}^{(2)} u_m + a_{11}\eta \left(\sum_{m=1}^N C_{im}^{(1)} w_m \sum_{m=1}^N C_{im}^{(2)} w_m + \sum_{m=1}^N C_{im}^{(2)} w_m \sum_{m=1}^N C_{im}^{(1)} w_m^* + \sum_{m=1}^N C_{im}^{(1)} w_m \sum_{m=1}^N C_{im}^{(2)} w_m^* \right) \\ + \sum_{m=1}^N C_{im}^{(2)} w_m \sum_{m=1}^N C_{im}^{(1)} w_{0m} + \sum_{m=1}^N C_{im}^{(1)} w_m \sum_{m=1}^N C_{im}^{(2)} w_{0m}^* \Big) = I_a \ddot{u}_i, \end{aligned} \quad (41)$$

$$\begin{aligned} a_{55} \left(\sum_{m=1}^N C_{im}^{(2)} w_m + \frac{1}{\eta} \sum_{m=1}^N C_{im}^{(1)} \varphi_m \right) + \left[a_{11}\eta \sum_{m=1}^N C_{im}^{(1)} u_{0m} + \frac{a_{11}\eta^2}{2} \left(\sum_{m=1}^N C_{im}^{(1)} w_{0m} \right)^2 + a_{11}\eta^2 \sum_{m=1}^N C_{im}^{(1)} w_{0m} \sum_{m=1}^N C_{im}^{(1)} w_m^* \right. \\ \left. - P^T - P^E - P \right] \sum_{m=1}^N C_{im}^{(2)} w_m + a_{11}\eta \left(\sum_{m=1}^N C_{im}^{(2)} u_m + \eta \sum_{m=1}^N C_{im}^{(1)} w_m \sum_{m=1}^N C_{im}^{(2)} w_m + \eta \sum_{m=1}^N C_{im}^{(2)} w_m \sum_{m=1}^N C_{im}^{(1)} w_m^* \right. \\ \left. + \eta \sum_{m=1}^N C_{im}^{(1)} w_m \sum_{m=1}^N C_{im}^{(2)} w_m^* + \eta \sum_{m=1}^N C_{im}^{(2)} w_m \sum_{m=1}^N C_{im}^{(1)} w_{0m} + \eta \sum_{m=1}^N C_{im}^{(1)} w_m \sum_{m=1}^N C_{im}^{(2)} w_{0m}^* \right) \\ \left(\sum_{m=1}^N C_{im}^{(1)} w_m + \sum_{m=1}^N C_{im}^{(1)} w_{0m} + \sum_{m=1}^N C_{im}^{(1)} w_m^* \right) + a_{11}\eta \left[\sum_{m=1}^N C_{im}^{(1)} u_m + \frac{\eta}{2} \left(\sum_{m=1}^N C_{im}^{(1)} w_m \right)^2 \right. \\ \left. + \eta \sum_{m=1}^N C_{im}^{(1)} w_m \sum_{m=1}^N C_{im}^{(1)} w_{0m} + \eta \sum_{m=1}^N C_{im}^{(1)} w_m \sum_{m=1}^N C_{im}^{(1)} w_m^* \right] \\ \left(\sum_{m=1}^N C_{im}^{(2)} w_m + \sum_{m=1}^N C_{im}^{(2)} w_{0m} + \sum_{m=1}^N C_{im}^{(2)} w_m^* \right) = I_a \ddot{w}_i, \end{aligned} \quad (42)$$

$$d_{11} \sum_{m=1}^N C_{im}^{(2)} \varphi_m - \frac{a_{55}}{\eta} \left(\sum_{m=1}^N C_{im}^{(1)} w_m + \frac{1}{\eta} \varphi_i \right) = I_c \ddot{\varphi}_i. \quad (43)$$

The boundary conditions (34) and (35) can also be

rewritten as

Hinged (H)

$$u_1 = 0, \quad w_1 = 0, \quad d_{11} \sum_{m=1}^N C_{1m}^{(1)} \varphi_m = 0, \quad \text{at } x = x_1, \quad (44)$$

$$u_N = 0, \quad w_N = 0, \quad d_{11} \sum_{m=1}^N C_{Nm}^{(1)} \varphi_m = 0, \quad \text{at } x = x_N; \quad (45)$$

Clamped (C)

$$u_1 = 0, \quad w_1 = 0, \quad \varphi_1 = 0, \quad \text{at } x = x_1, \quad (46)$$

$$u_N = 0, \quad u_N = 0, \quad \varphi_N = 0, \quad \text{at } x = x_N. \quad (47)$$

In view of Eqs. (13) and (14) and keeping Eq. (27) in mind, incorporation of boundary conditions from Eqs. (44)-(47) into Eqs. (38)-(40) gives the matrix system of nonlinear algebraic equations that describes the thermo-electro-mechanical postbuckling of piezoelectric CNTRC beams as

$$(\mathbf{K}_L - \Delta T \mathbf{K}_T - V_Z \mathbf{K}_E - P \mathbf{K}_M + \mathbf{K}_{NL1} + \mathbf{K}_{NL2}) \mathbf{d} = \mathbf{R} \quad (48)$$

where \mathbf{d} represents the unknown displacement vector that is composed of u_i, w_i, φ_i ; the right-hand side vector \mathbf{R} is caused by the thermo-electro-mechanical load and geometric imperfections and will automatically vanish for perfect beams (i.e., $w^* = 0$); \mathbf{K}_L is the stiffness matrix, \mathbf{K}_T , \mathbf{K}_E and \mathbf{K}_M are the geometric stiffness matrices that are associated with the temperature change, actuator voltage and in-plane force, respectively. The elements in \mathbf{K}_{NL1} and \mathbf{K}_{NL2} are linearly and quadratically dependent on unknown displacements.

Likewise, letting $\mathbf{d} = \mathbf{d}^* e^{i\omega\tau}$ and removing the nonlinear terms in Eqs. (41)-(43), we arrive at the matrix system of linear algebraic equations governing the free vibration of thermo-electro-mechanically postbuckled piezoelectric CNTRC beam as

$$[\mathbf{K}_L - \Delta T \mathbf{K}_T - V_Z \mathbf{K}_E - (P - P_0) \mathbf{K}_M - \omega^2 \mathbf{M}] \mathbf{d}^* = \mathbf{0} \quad (49)$$

where \mathbf{M} is the mass matrix, P_0 is the internal force caused by the postbuckling deformation and is given by

$$P_0 = a_{11} \eta u_{0,x} + \frac{1}{2} a_{11} \eta^2 (w_{0,x})^2 + a_{11} \eta^2 w_{0,x} w_{*,x}^* \quad (50)$$

Note that the elements of \mathbf{K}_L in Eq. (49) are associated with the postbuckling deflection w_0 and therefore are not identical to those of \mathbf{K}_L in Eq. (48). In order to solve the free vibration problem of postbuckled piezoelectric CNTRC beams, the static postbuckling configuration is first determined by solving Eq. (48) using the modified Newton-Raphson technique as detailed in Wu *et al.* (2016c), after which the natural frequencies of piezoelectric CNTRC beams in the postbuckled state can be obtained by solving Eq. (49) through a standard eigenvalue algorithm.

3. Numerical results and discussion

In present analysis, the CNTRC host is made from a mixture of PMMA matrix and (10, 10) single-walled carbon nanotube (SWCNT) reinforcements. Their material properties are temperature-dependent and given as follows (Shen *et al.* 2017)

$$\begin{aligned} E_m &= (3.52 - 0.0034T) \text{ GPa}, \\ \alpha_m &= 45(1 + 0.0005\Delta T) \times 10^{-6} \text{ K}^{-1}, \\ \rho_m &= 1150 \text{ kg m}^{-3}, \quad \nu_m = 0.34 \end{aligned} \quad (51)$$

$$\begin{aligned} E_{11}^{\text{cn}} &= (6.18387 - 0.00286T + 4.22867 \times 10^{-6} T^2 \\ &\quad - 2.2724 \times 10^{-9} T^3) \text{ TPa}, \\ E_{22}^{\text{cn}} &= (7.75348 - 0.00358T + 5.30057 \times 10^{-6} T^2 \\ &\quad - 2.84868 \times 10^{-9} T^3) \text{ TPa}, \\ G_{12}^{\text{cn}} &= (1.80126 + 7.7845 \times 10^{-4} T - 1.1279 \times 10^{-6} T^2 \\ &\quad + 4.93484 \times 10^{-10} T^3) \text{ TPa}, \\ \alpha_{11}^{\text{cn}} &= (-1.12148 + 0.02289T - 2.88155 \times 10^{-5} T^2 \\ &\quad + 1.13253 \times 10^{-8} T^3) \times 10^{-6} \text{ K}^{-1}, \\ \rho_m &= 1400 \text{ kg m}^{-3}, \quad \nu_m = 0.175. \end{aligned} \quad (52)$$

The CNT efficiency parameters η_i used in Eqs. (2)-(4) are determined by matching the Young's moduli and shear modulus of CNTRCs calculated from the rule of mixture to those obtained from the molecular dynamics simulation (Han and Elliott 2007). As reported by Shen and Zhang (2010), $\eta_1 = 0.137$, $\eta_2 = 1.022$, $\eta_3 = 0.715$ for $V_{\text{cn}}^* = 0.12$, $\eta_1 = 0.142$, $\eta_2 = 1.626$, $\eta_3 = 1.138$ for $V_{\text{cn}}^* = 0.17$, and $\eta_1 = 0.141$, $\eta_2 = 1.585$, $\eta_3 = 1.109$ for $V_{\text{cn}}^* = 0.28$. The piezoelectric layers are assumed to be temperature-independent with $E_p = 63.0$ GPa, $\alpha_p = 0.9 \times 10^{-6} \text{ K}^{-1}$, $d_{31} = 2.54 \times 10^{-10} \text{ m V}^{-1}$, $\rho_p = 7600 \text{ kg m}^{-3}$ and $\nu_p = 0.3$.

3.1 Convergence and comparison studies

Convergence and comparison studies are first conducted to validate the present formulations and solution method. The dimensionless postbuckling deflections at varying number of grid points N are calculated and compared in Table 2 for imperfect piezoelectric FGX-CNTRC beams under a given thermo-electro-mechanical load. w_c is the dimensionless deflection at the beam center. The minimum number of grid points required to obtain convergent results increases with the number of half-waves in the imperfection. This is because the imperfection containing more half-wave numbers has a more complex geometry which requires more grid points to represent. For simplicity, $N = 39$ is used in all the subsequent studies.

Comparison study is performed by considering the free vibration of a thermally postbuckled isotropic homogeneous beam with different boundary conditions. The fundamental frequency versus temperature rise curves are depicted and

Table 2 Convergence of dimensionless postbuckling deflection w_c for H-H piezoelectric FGX-CNTRC beams with different geometric imperfections ($V_{cn}^* = 0.17$, $L/H = 60$, $h_p/h = 1/10$, $\Delta T = 130$ K, $V_z = -200$ V, $P/P_{cr} = 0.2$, $A_0 = 0.1$)

N	Imperfection mode								
	Sine	G1	G2	G3	G4	L1	L2	L3	L4
9	2.280	2.247	2.362	2.943	2.818	2.385	2.403	2.433	2.414
15	2.280	2.247	2.344	2.337	2.497	2.346	2.363	2.435	2.573
21	2.280	2.247	2.344	2.335	2.333	2.329	2.337	2.367	2.450
27	2.280	2.247	2.344	2.335	2.332	2.322	2.326	2.337	2.359
33	2.280	2.247	2.344	2.335	2.332	2.321	2.325	2.332	2.338
39	2.280	2.247	2.344	2.335	2.332	2.321	2.324	2.330	2.334
45	2.280	2.247	2.344	2.335	2.332	2.321	2.324	2.330	2.334
51	2.280	2.247	2.344	2.335	2.332	2.321	2.324	2.330	2.334

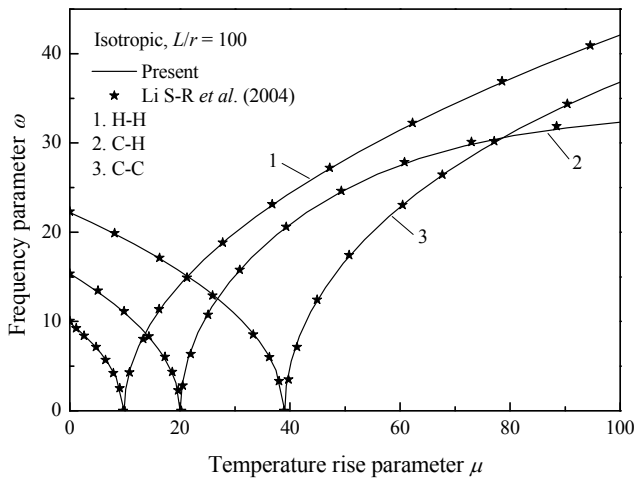


Fig. 2 Comparison of fundamental frequency for a thermally postbuckled isotropic homogeneous beam

compared in Fig. 2 with those given by Li *et al.* (2004) using the shooting method. Our results are in good agreement with those reported in the literature.

3.2 Thermal postbuckling

This section studies the thermal postbuckling of piezoelectric FG-CNTRC beams that are initially stressed by a constant actuator voltage and an in-plane force. Unless otherwise mentioned, the thermal postbuckling results, in the form of the temperature rise ΔT (K) plotted against the dimensionless central deflection w_c , are presented in Figs. 3-9 for H-H FGX-CNTRC hybrid beams with $L/H = 60$, $h_p/h = 1/10$, $V_{cn}^* = 0.17$, $A_0 = 0.1$, $V_z = -200$ V and $P = 0.2P_{cr}$, where P_{cr} is the compressive critical buckling load of the perfect hybrid beam at $\Delta T = 0$ K.

Figs. 3 and 4 investigate the effects of CNT distribution pattern and volume fraction on the thermal postbuckling behaviour of piezoelectric FG-CNTRC beams that contain a sine type imperfection. The distribution pattern FGX with more CNT reinforcements dispersed near the surfaces of the CNTRC host is capable of carrying a higher temperature in the postbuckling stage than the patterns UD and FGO. The

thermal postbuckling curve becomes lower as the CNT volume fraction increases, which is opposite of the observation for the beam without piezoelectric layers and in-plane force (Wu *et al.* 2017). This is because the beam with more CNTs possesses a greater buckling load P_{cr} and therefore is subjected to a higher in-plane force ($P = 0.2P_{cr}$) that significantly weakens the beam stiffness. It is worthy to note that bifurcation buckling does not occur due to the presence of the initial deflection in imperfect beams. Moreover, the thermal postbuckling load-deflection curve of an imperfect beam is lower than that of its perfect counterpart at a certain range of deflection but gets higher when the deflection is sufficiently large.

The influence of half-wave number on the thermal postbuckling behaviour of FGX-CNTRC hybrid beams is examined in Figs. 5(a) and (b) where the global and localized imperfections are considered, respectively. The half-wave number b is 2, 3, 5, 7 for G1 (L1) - G4 (L4) in order. The results show that the thermal postbuckling response is less affected by the imperfection with more half-waves. To be specific, the postbuckling curves of globally imperfect beams are almost overlapped and extremely close to that of the perfect counterpart when the

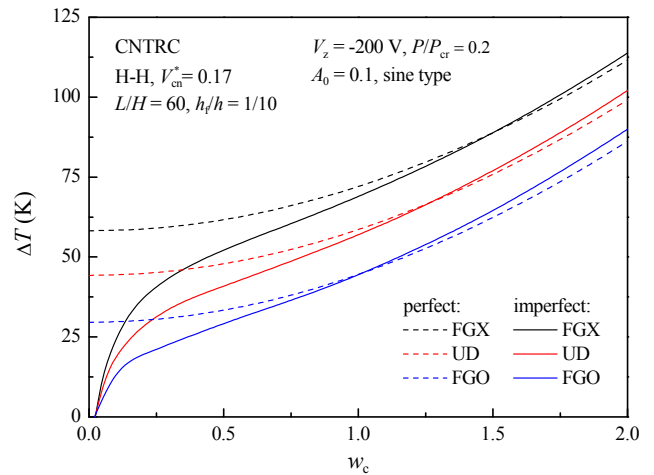


Fig. 3 Effect of CNT distribution pattern on the thermal postbuckling of piezoelectric FG-CNTRC beams

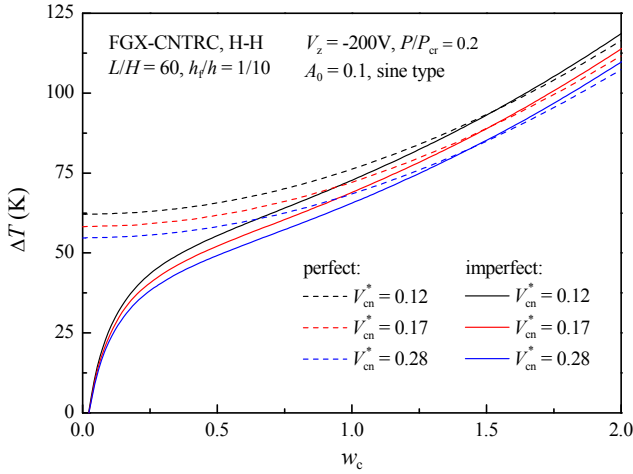


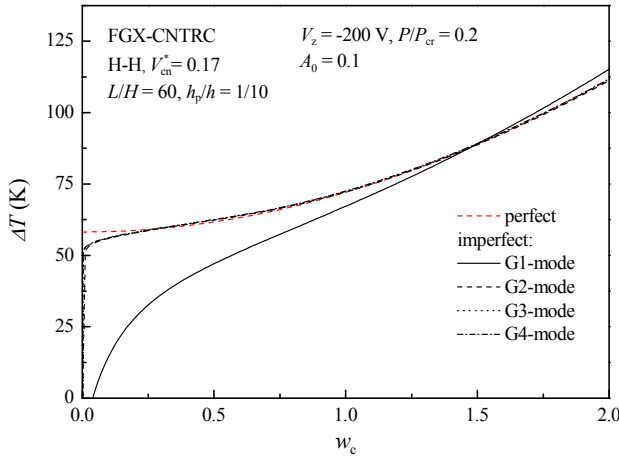
Fig. 4 Effect of CNT volume fraction on the thermal postbuckling of piezoelectric FGX-CNTRC beams

half-wave number is more than 2, while the curves of locally imperfect beams gradually approach that of the

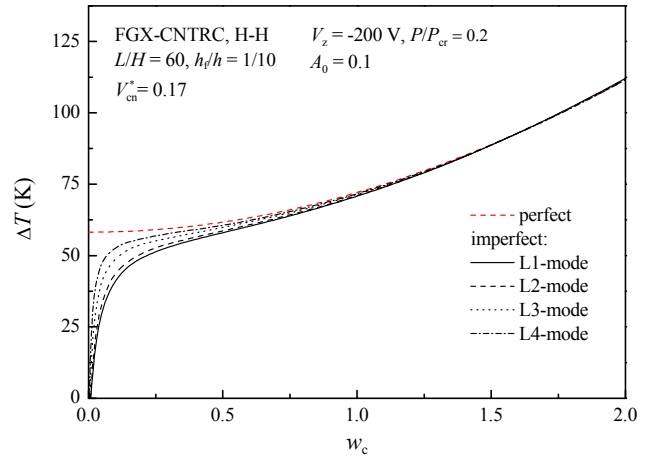
perfect counterpart as the half-wave number increases.

Fig. 6 compares the thermal postbuckling paths of FGX-CNTRC hybrid beams with either a G1-mode or an L1-mode imperfection whose center is located at $x = 0.1, 0.2, 0.3, 0.4, 0.5$ (i.e., $c = 0.1, 0.2, 0.3, 0.4, 0.5$). Among those, $c = 0.5$ means the imperfection geometry is symmetric about the beam center $x = 0.5$. The difference between the thermal postbuckling curves of perfect and imperfect beams is more significant as the imperfection center move towards the beam end. The thermal postbuckling curves of G1-mode shaped beams with $c = 0.1$ and 0.2 are symmetrical to those with $c = 0.4$ and 0.3 , respectively. This is due to the fact that the geometries of G1-mode imperfections at $c = 0.1$ and 0.2 are antisymmetric with those at $c = 0.4$ and 0.3 .

The effects of imperfection amplitude are examined in Figs. 7(a), (b) and (c) where the sine type, G1-mode and L1-mode imperfections are considered, respectively. The FGX-CNTRC hybrid beam with a higher imperfection amplitude tends to carry a lower temperature rise within a certain range of deflection, beyond which the imperfection

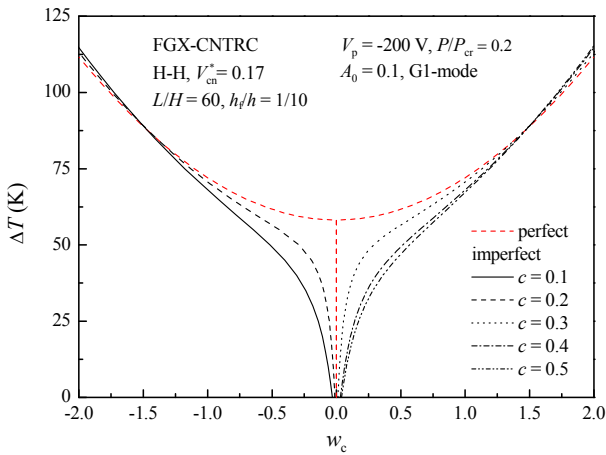


(a) Global imperfections

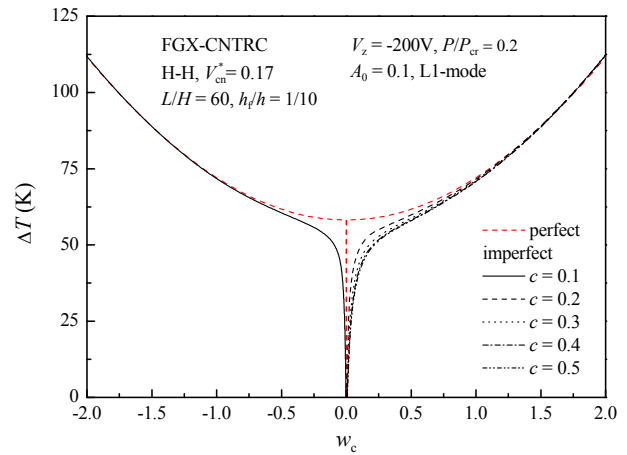


(b) Localized imperfections

Fig. 5 Effect of imperfection half-wave number on the thermal postbuckling of piezoelectric FGX-CNTRC beams



(a) G1-mode



(b) L1-mode

Fig. 6 Effect of imperfection location on the thermal postbuckling of piezoelectric FGX-CNTRC beams

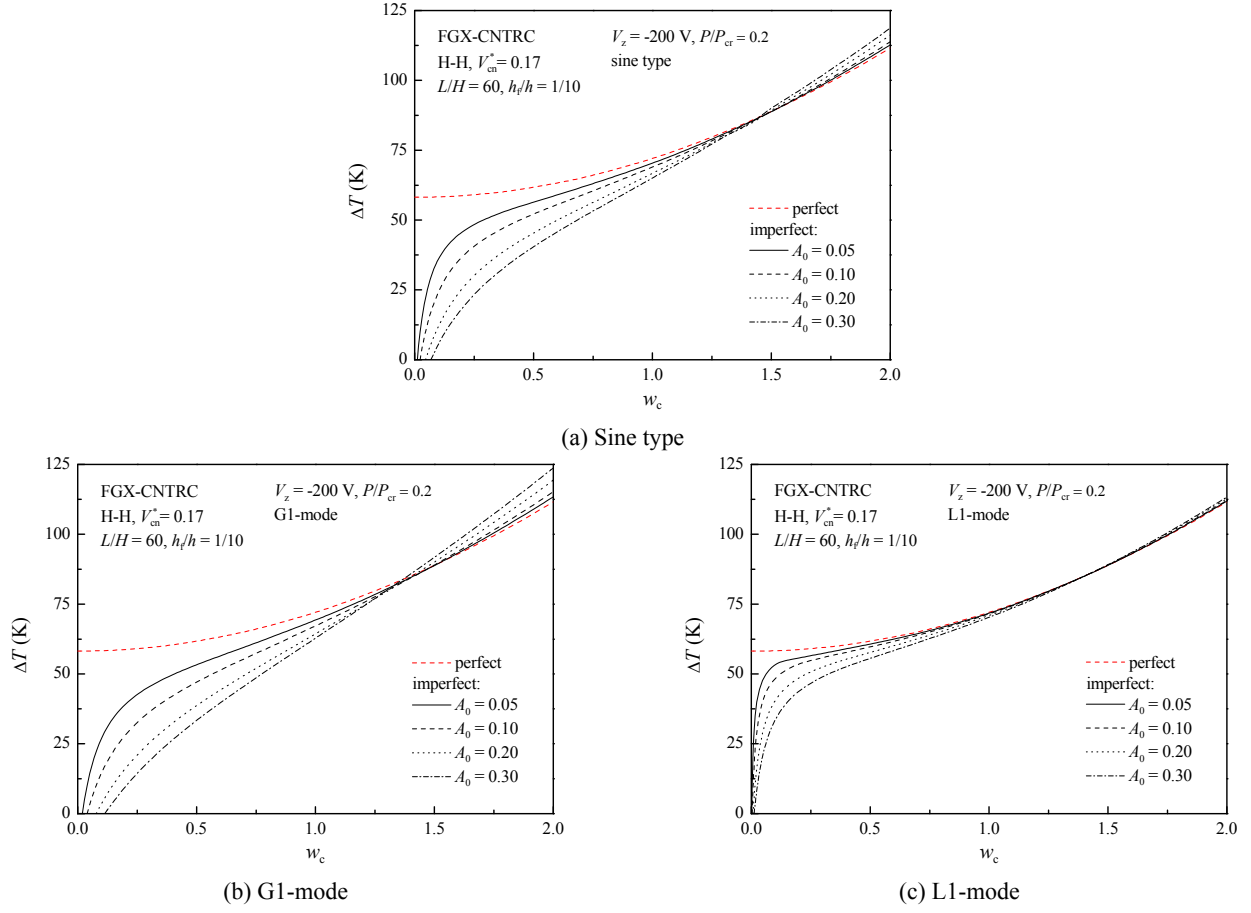


Fig. 7 Effect of imperfection amplitude on the thermal postbuckling of piezoelectric FGX-CNTRC beams

amplitude has the opposite effect. By comparing the curves in the figures, the thermal postbuckling is most affected by G1-mode imperfection, followed by the sine type and L1-mode imperfections.

Figs. 8 and 9 evaluate the influences of the applied voltage and in-plane force on the thermal postbuckling of FGX-CNTRC hybrid beams, respectively. A positive/negative value of P/P_{cr} represents a compressive/tensile

force exerted on the beam. Both the negative voltage and tensile force increase the beam stiffness thus lead to a higher thermal postbuckling resistance, while the positive voltage and compressive force have inverse effects. It should be noted in Fig. 9 that the postbuckling curves of $P/P_{cr} = -0.2$ and 0.0 do not start from $\Delta T = 0$ K due to the negative initial deflection caused by the electro-mechanical load in these two cases.

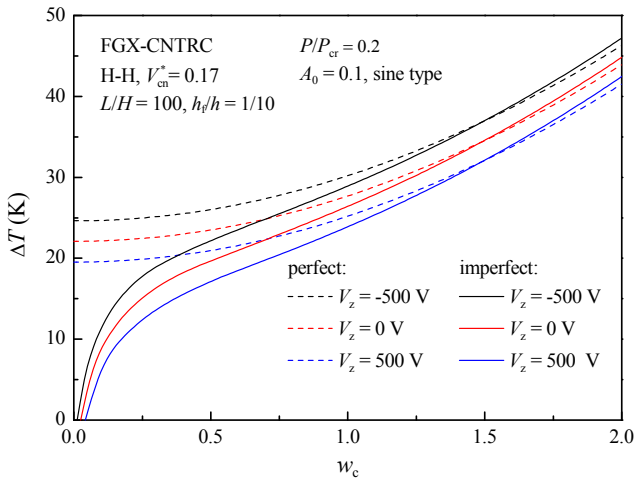


Fig. 8 Effect of actuator voltage on the thermal postbuckling of piezoelectric FGX-CNTRC beams

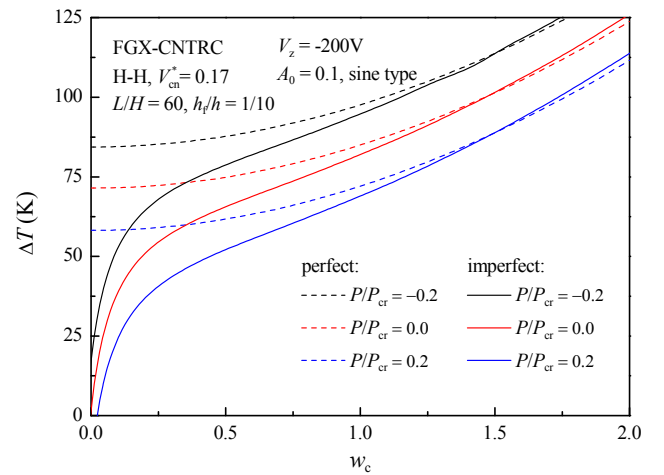


Fig. 9 Effect of in-plane force on the thermal postbuckling of piezoelectric FGX-CNTRC beams

3.3 Free vibration

We next turn our attention to the free vibration analysis of thermo-electro-mechanically postbuckled piezoelectric FG-CNTRC beams. Numerical results, in terms of the dimensionless fundamental frequency ω against the temperature rise ΔT (K), are given in Figs. 10-17 for both perfect and imperfect FG-CNTRC hybrid beams with various parameters, where the intersection at $\omega = 0$ represents the critical buckling temperature rise ΔT_{cr} of perfect hybrid beams.

The results in Figs. 10-17 show that the fundamental frequencies are first reduced with the temperature rise due to the decrease in beam stiffness. As the temperature further increases, the growing thermal postbuckling deflection improves the nonlinear stiffness and the fundamental frequencies are then raised. The frequencies of perfect

beams become zero when $\Delta T = \Delta T_{cr}$ at which the curves are continuous but not smooth. This is because the configurations of perfect beams in the prebuckled and postbuckled states are totally different. However, the curves of imperfect beams are smooth and their fundamental frequencies are higher than those of perfect counterparts in the whole range of ΔT . This tends to be much more prominent as the temperature approaches the critical buckling temperature.

Figs. 10 and 11 present the variation of fundamental frequency with the temperature rise for piezoelectric FG-CNTRC beams with different CNT distribution patterns and volume fractions, respectively. The FGX-CNTRC hybrid beam has the highest fundamental frequency in the prebuckling temperature range, followed by the UD- and FGO-CNTRC ones. This is inversed in the postbuckling temperature range. The results also show that the fundamental frequency of imperfect beams increases in the whole temperature range as the CNT volume fraction increases, while the opposite effect is observed for perfect beams when ΔT is slightly less than ΔT_{cr} .

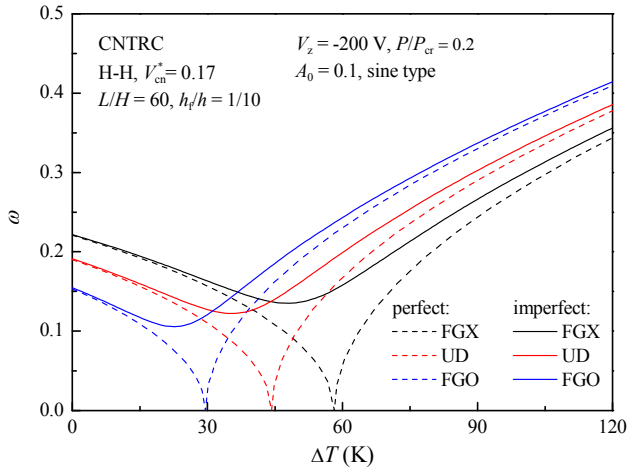


Fig. 10 Effect of CNT distribution pattern on the fundamental frequency of thermo-electro-mechanically postbuckled piezoelectric FG-CNTRC beams

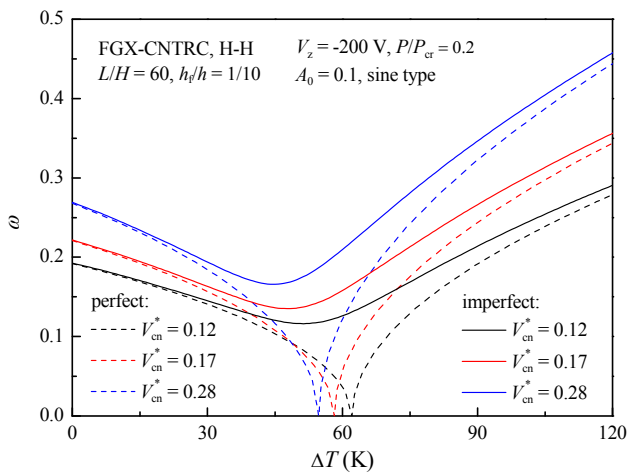
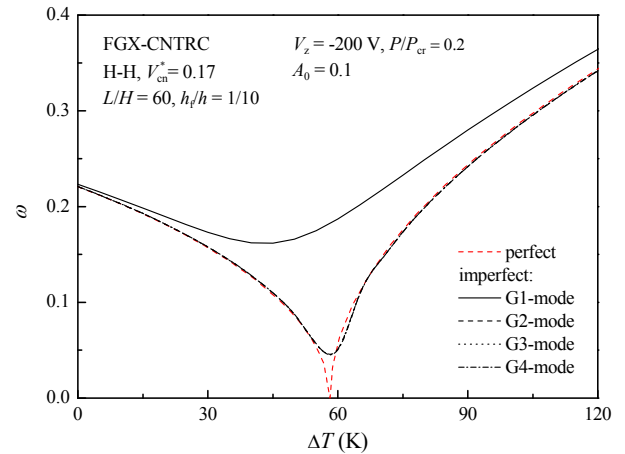
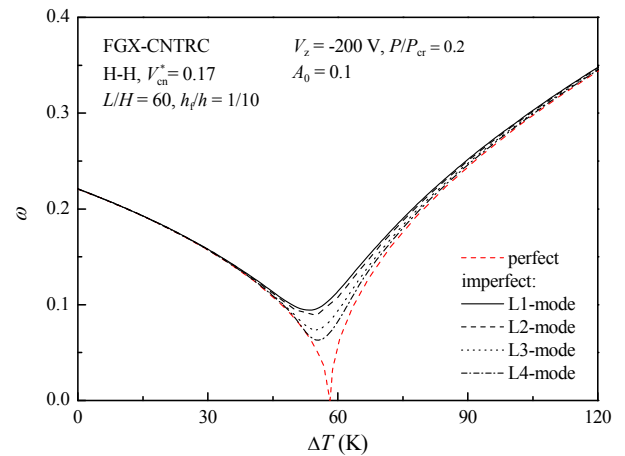


Fig. 11 Effect of CNT volume fraction on the fundamental frequency of thermo-electro-mechanically postbuckled piezoelectric FGX-CNTRC beams



(a) Global imperfections



(b) Localized imperfections

Fig. 12 Effect of imperfection half-wave number on the fundamental frequency of thermo-electro-mechanically postbuckled piezoelectric FGX-CNTRC beams

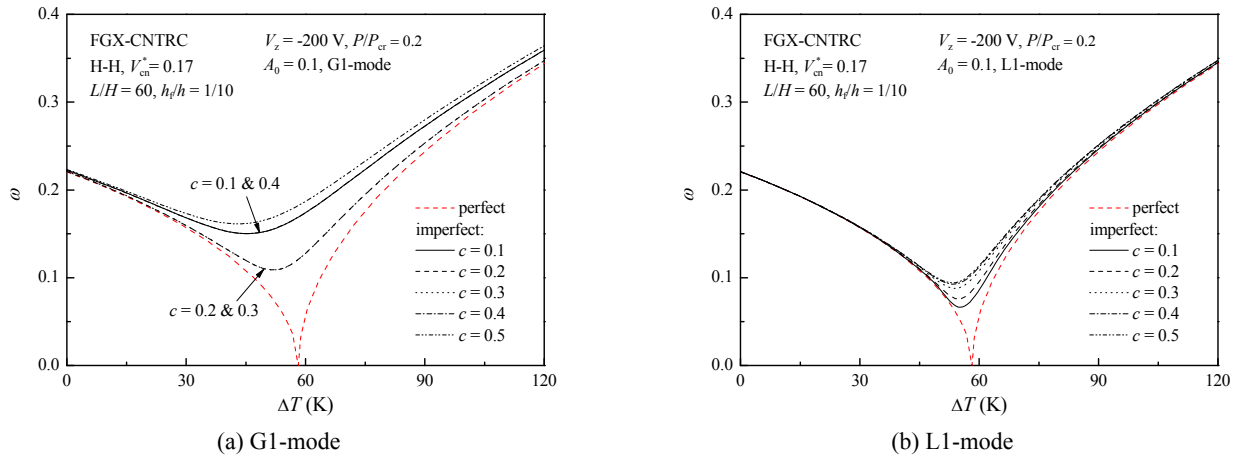


Fig. 13 Effect of imperfection location on the fundamental frequency of thermo-electro-mechanically postbuckled piezoelectric FGX-CNTRC beams

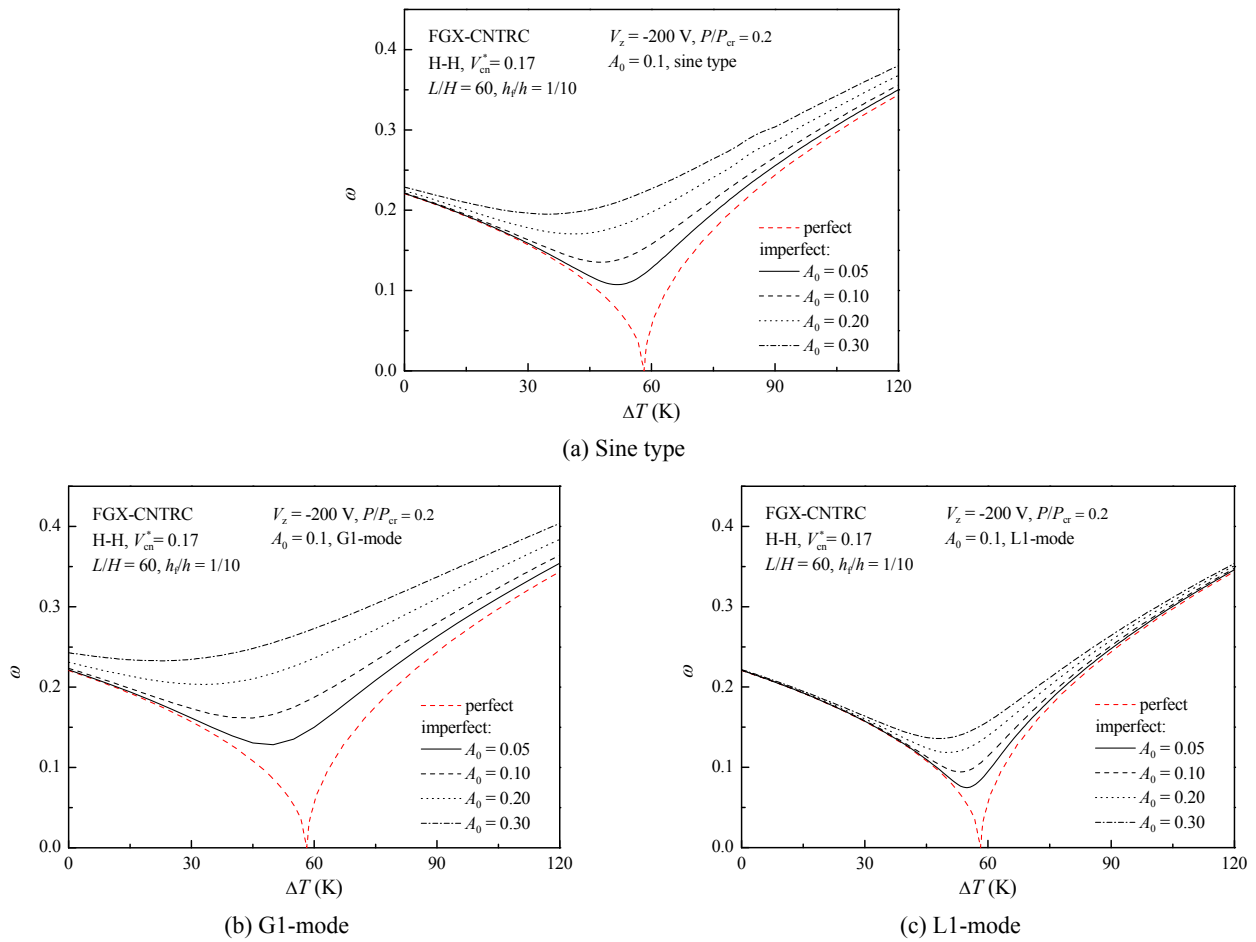


Fig. 14 Effect of imperfection amplitude on the fundamental frequency of thermo-electro-mechanically postbuckled piezoelectric FGX-CNTRC beams

Fig. 12 shows the effect of half-wave number on the fundamental frequency of FGX-CNTRC hybrid beams with either global or local imperfections. The results of the perfect beam are also given for a direct comparison. The half-wave number exhibits a similar effect on the fundamental frequency as on the thermal postbuckling. The fundamental frequency is considerably affected by the

global imperfection when the half-wave number $b = 2$, beyond which the global imperfection has almost no impact on the fundamental frequency. In contrast, the curve of a locally imperfect beam is continuously closer to that of the perfect counterpart as the half-wave number increases.

The influence of imperfection location on the fundamental frequency of FGX-CNTRC hybrid beams is

examined in Figs. 13(a) and (b) where the G1-mode and L1-mode imperfections are considered, respectively. The fundamental frequency is the highest when the imperfection is symmetrical about the beam center. The curves of imperfect beams containing a G1-mode imperfection with $c = 0.1$ and 0.2 coincide with those of $c = 0.4$ and 0.3 , respectively. This is attributed to the antisymmetry of their postbuckling configurations. However, the curve of the L1-mode featured beam becomes closer to that of the perfect beam when the imperfection center moves towards the beam end.

The fundamental frequency versus temperature rise curves are compared in Fig. 14 for FGX-CNTRC hybrid beams with different imperfection amplitudes. Three different imperfections, i.e., sine type, G1-mode and L1-mode, are considered in this example. The results indicate that the fundamental frequency increases as the imperfection amplitude grows. This effect is most pronounced for the G1-mode imperfection, followed by the sine type and L1-mode imperfections.

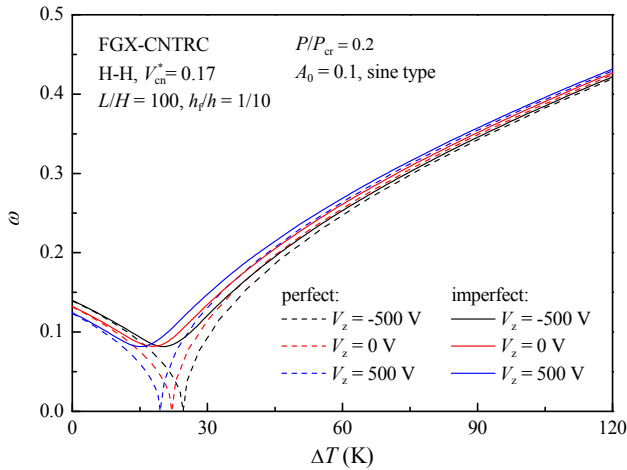


Fig. 15 Effect of applied voltage on the fundamental frequency of thermo-electro-mechanically postbuckled piezoelectric FGX-CNTRC beams

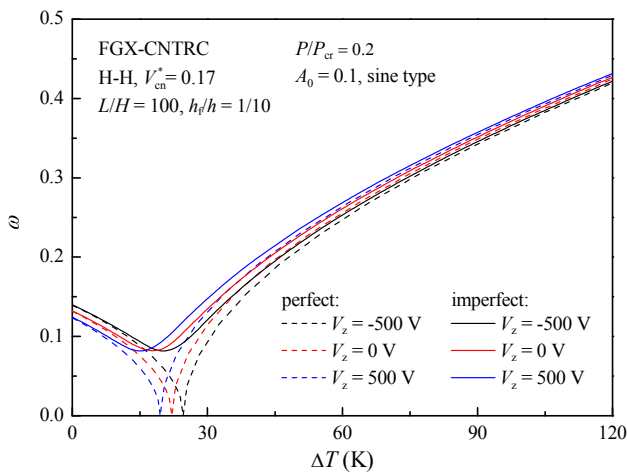


Fig. 16 Effect of in-plane force on the fundamental frequency of thermo-electro-mechanically postbuckled piezoelectric FGX-CNTRC beams

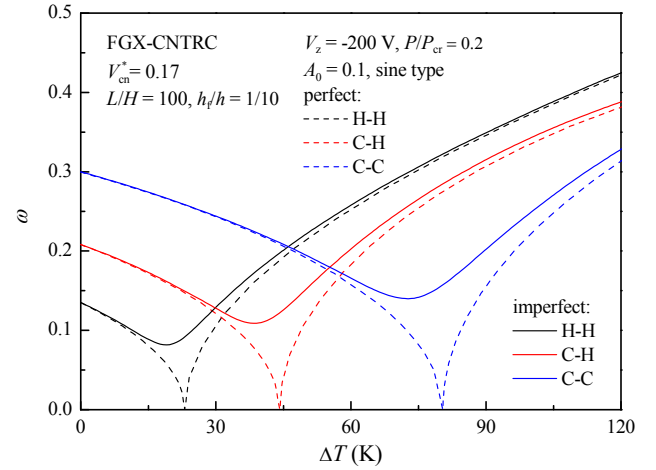


Fig. 17 Effect of boundary condition on the fundamental frequency of thermo-electro-mechanically postbuckled piezoelectric FGX-CNTRC beams

Figs. 15 and 16 demonstrate the effects of applied voltage and in-plane force on the fundamental frequency of FGX-CNTRC hybrid beams, respectively. The fundamental frequency increases in the prebuckling temperature range but decreases in the postbuckling temperature range when the beam is subjected to either a negative voltage or a tensile in-plane force. The reason is illustrated in Figs. 8 and 9, which show that the beam under a negative voltage/tensile force has a smaller postbuckling deflection and therefore possesses a lower nonlinear stiffness in the postbuckling temperature range.

Fig. 17 depicts the variation of fundamental frequency with the temperature rise for FGX-CNTRC hybrid beams with different boundary conditions. The fundamental frequency of the H-H beam is smaller in the prebuckling temperature range due to the lower supporting rigidity but is greater in the postbuckling temperature range because of the higher nonlinear stiffness, followed by the C-H and C-C beams. The relatively larger difference between the curves of perfect and imperfect beams indicates that the fundamental frequency of the C-C beam is more sensitive to the imperfection.

4. Conclusions

The free vibration of thermo-electro-mechanically postbuckled piezoelectric FG-CNTRC hybrid beams with geometric imperfections is studied in this paper within the framework of FSDT. The DQ method in conjunction with Newton-Raphson technique is used to obtain the fundamental frequencies of FG-CNTRC hybrid beams in the postbuckled states. Thermo-electro-mechanical postbuckling of such a beam is also analyzed as a subset problem. Comprehensive numerical results are presented in graphical form to illustrate the influences of CNT distribution pattern and volume fraction, geometric imperfection parameters, thermo-electro-mechanical load and boundary condition on the postbuckling and free vibration behaviours of the beam. Our results show that the

fundamental frequencies of geometrically imperfect FG-CNTRC hybrid beams are higher than those of perfect counterparts and this effect is much more pronounced around the critical buckling temperature. The imperfection with fewer half-waves but a larger amplitude leads to a higher fundamental frequency that is most increased when the imperfection is symmetrical about the beam center. In addition, the fundamental frequency is raised/reduced in the prebuckling/postbuckling temperature range when the beam is subjected to either a negative voltage or a tensile force, while the positive voltage and compressive force have inverse effects. The results also indicate that the CNT distribution pattern and volume fraction have significant impacts on the free vibration of postbuckled piezoelectric FG-CNTRC beams.

Acknowledgments

The work described in this paper was fully funded by two research grants from the Australian Research Council under Discovery Project scheme (DP160101978, DP140102132). The authors are grateful for their financial support.

References

- Alibeigloo, A. and Liew, K. (2015), "Elasticity solution of free vibration and bending behavior of functionally graded carbon nanotube-reinforced composite beam with thin piezoelectric layers using differential quadrature method", *Int. J. Appl. Mech.*, **7**(1), 1550002.
- Asadi, H., Bodaghi, M., Shakeri, M. and Aghdam, M.M. (2013), "On the free vibration of thermally pre/post-buckled shear deformable SMA hybrid composite beams", *Aerosp. Sci. Technol.*, **31**(1), 73-86.
- Duan, W.H., Wang, Q. and Quek, S.T. (2010), "Applications of piezoelectric materials in structural health monitoring and repair: Selected research examples", *Materials*, **3**(12), 5169-5194.
- Emam, S.A. (2009), "A static and dynamic analysis of the postbuckling of geometrically imperfect composite beams", *Compos. Struct.*, **90**(2), 247-253.
- Esfahani, S., Kiani, Y., Komijani, M. and Eslami, M. (2014), "Vibration of a temperature-dependent thermally pre/postbuckled FGM beam over a nonlinear hardening elastic foundation", *J. Appl. Mech.*, **81**(1), 011004.
- Han, Y. and Elliott, J. (2007), "Molecular dynamics simulations of the elastic properties of polymer/carbon nanotube composites", *Compos. Mater. Sci.*, **39**(2), 315-323.
- Ke, L.L., Yang, J. and Kitipornchai, S. (2010), "Nonlinear free vibration of functionally graded carbon nanotube-reinforced composite beams", *Compos. Struct.*, **92**(3), 676-683.
- Komijani, M., Kiani, Y., Esfahani, S.E. and Eslami, M.R. (2013), "Vibration of thermo-electrically post-buckled rectangular functionally graded piezoelectric beams", *Compos. Struct.*, **98**, 143-152.
- Komijani, M., Esfahani, S.E., Reddy, J.N., Liu, Y.P. and Eslami, M.R. (2014), "Nonlinear thermal stability and vibration of pre/post-buckled temperature- and microstructure-dependent functionally graded beams resting on elastic foundation", *Compos. Struct.*, **112**, 292-307.
- Li, S.-R., Teng, Z.-C. and Zhou, Y.-H. (2004), "Free vibration of heated Euler-Bernoulli beams with thermal postbuckling deformations", *J. Therm. Stress.*, **27**(9), 843-856.
- Li, S.-R., Su, H.-D. and Cheng, C.-J. (2009), "Free vibration of functionally graded material beams with surface-bonded piezoelectric layers in thermal environment", *Appl. Math. Mech.-Eng. Ed.*, **30**(8), 969-982.
- Liew, K.M., Lei, Z.X. and Zhang, L.W. (2015), "Mechanical analysis of functionally graded carbon nanotube reinforced composites: A review", *Compos. Struct.*, **120**, 90-97.
- Lin, F. and Xiang, Y. (2014a), "Numerical analysis on nonlinear free vibration of carbon nanotube reinforced composite beams", *Int. J. Struct. Stab. Dy.*, **14**(1), 1350056.
- Lin, F. and Xiang, Y. (2014b), "Vibration of carbon nanotube reinforced composite beams based on the first and third order beam theories", *Appl. Math. Model.*, **38**(15), 3741-3754.
- Nejati, M., Eslampanah, A. and Najafizadeh, M. (2016), "Buckling and Vibration Analysis of Functionally Graded Carbon Nanotube-Reinforced Beam Under Axial Load", *Int. J. Appl. Mech.*, **8**(1), 1650008.
- Rafiee, M., Yang, J. and Kitipornchai, S. (2013a), "Large amplitude vibration of carbon nanotube reinforced functionally graded composite beams with piezoelectric layers", *Compos. Struct.*, **96**, 716-725.
- Rafiee, M., Yang, J. and Kitipornchai, S. (2013b), "Thermal bifurcation buckling of piezoelectric carbon nanotube reinforced composite beams", *Comput. Math. Appl.*, **66**(7), 1147-1160.
- Rahimi, G., Gazor, M., Hemmatnezhad, M. and Toorani, H. (2013), "On the postbuckling and free vibrations of FG Timoshenko beams", *Compos. Struct.*, **95**, 247-253.
- Shen, H.-S. (2009), "Nonlinear bending of functionally graded carbon nanotube-reinforced composite plates in thermal environments", *Compos. Struct.*, **91**(1), 9-19.
- Shen, H.-S. and Zhang, C.-L. (2010), "Thermal buckling and postbuckling behavior of functionally graded carbon nanotube-reinforced composite plates", *Mater. Des.*, **31**(7), 3403-3411.
- Shen, H.-S. and Xiang, Y. (2013), "Nonlinear analysis of nanotube-reinforced composite beams resting on elastic foundations in thermal environments", *Eng. Struct.*, **56**, 698-708.
- Shen, H.-S., He, X.Q. and Yang, D.-Q. (2017), "Vibration of thermally postbuckled carbon nanotube-reinforced composite beams resting on elastic foundations", *Int. J. Nonlin. Mech.*, **91**, 69-75.
- Wadee, M.A. (2000), "Effects of periodic and localized imperfections on struts on nonlinear foundations and compression sandwich panels", *Int. J. Solids. Struct.*, **37**(8), 1191-1209.
- Wattanasakulpong, N. and Ungbhakorn, V. (2013), "Analytical solutions for bending, buckling and vibration responses of carbon nanotube-reinforced composite beams resting on elastic foundation", *Compos. Mater. Sci.*, **71**, 201-208.
- Wu, H.L., Kitipornchai, S. and Yang, J. (2015), "Free vibration and buckling analysis of sandwich beams with functionally graded carbon nanotube-reinforced composite face sheets", *Int. J. Struct. Stab. Dy.*, **15**(7), 1540011.
- Wu, H.L., Yang, J. and Kitipornchai, S. (2016a), "Imperfection sensitivity of postbuckling behaviour of functionally graded carbon nanotube-reinforced composite beams", *Thin-Wall. Struct.*, **108**, 225-233.
- Wu, H.L., Yang, J. and Kitipornchai, S. (2016b), "Nonlinear vibration of functionally graded carbon nanotube-reinforced composite beams with geometric imperfections", *Compos. Part B-Eng.*, **90**, 86-96.
- Wu, H.L., Kitipornchai, S. and Yang, J. (2016c), "Thermo-electro-mechanical postbuckling of piezoelectric FG-CNTRC beams with geometric imperfections", *Smart Mater. Struct.*, **25**(9), 095022.

- Wu, H.L., Kitipornchai, S. and Yang, J. (2017), "Imperfection sensitivity of thermal post-buckling behaviour of functionally graded carbon nanotube-reinforced composite beams", *Appl. Math. Model.*, **42**, 735-752.
- Yang, J., Liew, K.M. and Kitipornchai, S. (2006), "Imperfection sensitivity of the post-buckling behavior of higher-order shear deformable functionally graded plates", *Int. J. Solids Struct.*, **43**(17), 5247-5266.
- Yang, J., Ke, L.-L. and Feng, C. (2015), "Dynamic buckling of thermo-electro-mechanically loaded FG-CNTRC beams", *Int. J. Struct. Stab. Dy.*, **15**(8), 1540017.
- Yas, M. and Samadi, N. (2012), "Free vibrations and buckling analysis of carbon nanotube-reinforced composite Timoshenko beams on elastic foundation", *Int. J. Press. Vessels Pip.*, **98**, 119-128.
- Zhang, L., Song, Z. and Liew, K. (2016), "Optimal shape control of CNT reinforced functionally graded composite plates using piezoelectric patches", *Compos. Part B-Eng.*, **85**, 140-149.

BU